



## ORIGINAL ARTICLE

# Enhanced catalytic activity of composites of $\text{NiFe}_2\text{O}_4$ and nano cellulose derived from waste biomass for the mitigation of organic pollutants



Kanu Gupta <sup>a</sup>, Anupama Kaushik <sup>b</sup>, K.B. Tikoo <sup>c</sup>, Vinod Kumar <sup>c</sup>, Sonal Singhal <sup>a,\*</sup>

<sup>a</sup> Department of Chemistry, Panjab University, Chandigarh 160014, India

<sup>b</sup> Dr. SSB UICET, Panjab University, Chandigarh 160014, India

<sup>c</sup> HRTEM Facility Lab, NIPER, Mohali, 160062 Punjab, India

Received 3 June 2017; accepted 27 July 2017

Available online 3 August 2017

## KEYWORDS

Cellulose nanofibres;  
Magnetically retrievable  
nanocomposites;  
Photocatalytic oxidation;  
Reduction

**Abstract** This study reports facile in situ synthesis of magnetically retrievable nanocomposites of nanocellulose (derived from waste biomass) and  $\text{NiFe}_2\text{O}_4$  nanoparticles using hydrothermal method. The synthesized nanocomposites were characterized using various techniques such as FT-IR, powder XRD, HR-TEM, BET and VSM. The characterization of nanocomposites clearly revealed that  $\text{NiFe}_2\text{O}_4$  nanoparticles were well dispersed on the surface of cellulose nanofibres. The catalytic performance of the synthesized nanocomposites was assessed for both the photocatalytic oxidation and reduction of organic pollutants. The prepared nanocomposites displayed excellent catalytic performance in comparison to pristine  $\text{NiFe}_2\text{O}_4$  nanoparticles due to stabilization and increased dispersability of  $\text{NiFe}_2\text{O}_4$  nanoparticles on the cellulose matrix. The present work promotes the use of bio based renewable sources to fabricate environment friendly materials to be used in the field of catalysis for the abatement of organic pollutants.

© 2017 The Authors. Production and hosting by Elsevier B.V. on behalf of King Saud University. This is an open access article under the CC BY-NC-ND license (<http://creativecommons.org/licenses/by-nc-nd/4.0/>).

## 1. Introduction

Recently ferrite based nanomaterials have emerged as a class of important functional materials because of their unique char-

acteristics like high surface area, large surface to volume ratio, strong adsorption capacity, facile recovery, etc. (Velinov et al., 2016; Polshettiwar et al., 2011; Casbeer et al., 2012). Owing to these unique characteristics, ferrite based nanomaterials have found potential applications in catalysis, drug delivery, water treatment, sensors, memory devices, electrical components, etc. (Yamaguchi et al., 2006; Sharma and Singhal, 2013; Harris et al., 2009). Out of all these fields, ferrite based nanomaterials have received prominent attention in the field of catalysis as these nanomaterials show significant enhancement in the catalytic activity. However the major drawback of using ferrites as catalyst is their problem of agglomeration. Due to their inherent magnetic character, the ferrites tend to agglom-

\* Corresponding author.

E-mail addresses: [sonal1174@gmail.com](mailto:sonal1174@gmail.com), [sonal@pu.ac.in](mailto:sonal@pu.ac.in) (S. Singhal).

Peer review under responsibility of King Saud University.



erate thereby reducing their dispersability and hence catalytic properties (Zhu et al., 2010). Thus the aggregation of ferrite nanoparticles must be prevented in order to exhibit their truly remarkable properties. In order to avoid aggregation, various organic and inorganic materials have been used as a template to load bare ferrite nanoparticles. These loaded nanoparticles are substantially more stable against aggregation due to large decrease in their surface energy as compared to bare nanoparticles (Rozenberg and Tenne, 2008). Various organic and inorganic matrixes like chitosan (Meng et al., 2015), carbon nanotubes (Datta et al., 2017), graphene (Xu et al., 2012), polyethylene (Parsons et al., 2014), etc. have been used to load bare ferrite nanoparticles to fabricate high performance nanocomposites.

Cellulose, being a green organic matrix, has emerged out to be an excellent template for the stabilisation of these reactive ferrite nanoparticles to fabricate organic/inorganic composite materials. This is due to the fact that cellulose exhibits high surface area wherein the inorganic particles can be attached on its surface by means of strong van der Waals interactions between the inorganic particles and various hydroxyl groups present on the surface of cellulose (Virkyte and Varma, 2011). Cellulose is a bio based almost inexhaustible resource and is a versatile starting material for the production of cellulose based materials and stable cellulose derivatives which can be used for domestic and commercial applications. The isolation, characterization and applications of various form of cellulose, including crystallites, nanocrystals, whiskers and nanofibers are being widely explored (Siró and Plackett, 2010). Cellulose nanofibers have been a focus of investigation because of its unique characteristics such as high surface area, good mechanical properties, large surface to volume ratio, unique morphology, nanoscale dimensions, etc. (Takagi and Asano, 2007; Nishino et al., 2004). All these features make cellulose nanofibers a promising material in the field of nanotechnology.

Nanocomposites present the best properties of each of the components in a synergic way (Sanchez et al., 2005). The synthesis of cellulose nanofibres and their applications in composite materials has gained profound attention due to their high strength and stiffness combined with low weight and biodegradability. Owing to its green and eco-friendly characteristic, cellulose based nanocomposites fit very well within the scope of sustainable and green chemistry perspectives. Diverse research has been going on the synthesis and studies of cellulose based nanocomposites and to evaluate their catalytic efficiency for various organic transformations, water treatment, metal removal, etc. (Galland et al., 2013; Liu et al., 2016; Yu et al., 2014) Xiong et al. (2014) reported the synthesis of magnetic nanocomposites of cellulose/ultrasmall iron oxide nanoparticles by co-precipitation method and used it as a catalyst for water treatment. The synthesized nanocomposite showed excellent adsorption capacity for Pb (II) and methylene blue and thereby promotes the use of bio based renewable resources for the fabrication of variety of composite materials to be used in diverse fields. Gopiraman et al. (2015) successfully decorated silver and ruthenium nanoparticles on the surface of cellulose acetate nanofibres. The synthesized nanocomposites showed excellent catalytic activity in the aerobic oxidation of benzyl alcohol and in aza-Michael reaction. Zhang et al. (2016) synthesized highly functionalized

adsorbent TEMPO-mediated oxidized cellulose nanofibrils modified with polyethyleneamine for Cu (II) adsorption.

Taking cognizance of the eco-friendly characteristics and excellent properties of cellulose based nanocomposites, present work encompasses the extraction of cellulose nanofibers (CNF) from bio-waste (pine needles) and further utilising these nanofibers to fabricate cellulose- NiFe<sub>2</sub>O<sub>4</sub> nanocomposites (CNF-NiFe) by the in-situ deposition of NiFe<sub>2</sub>O<sub>4</sub> (NiFe) nanoparticles on the surface of CNF. Silanization of CNF (SCNF) has also been done to fabricate SCNF-NiFe nanocomposites. The catalytic efficiency of the synthesized nanocomposites has been evaluated by carrying out the photo-Fenton degradation of pollutant dye Remazol Black 5 and reduction of nitroaromatic phenols.

## 2. Experimental section

### 2.1. Materials

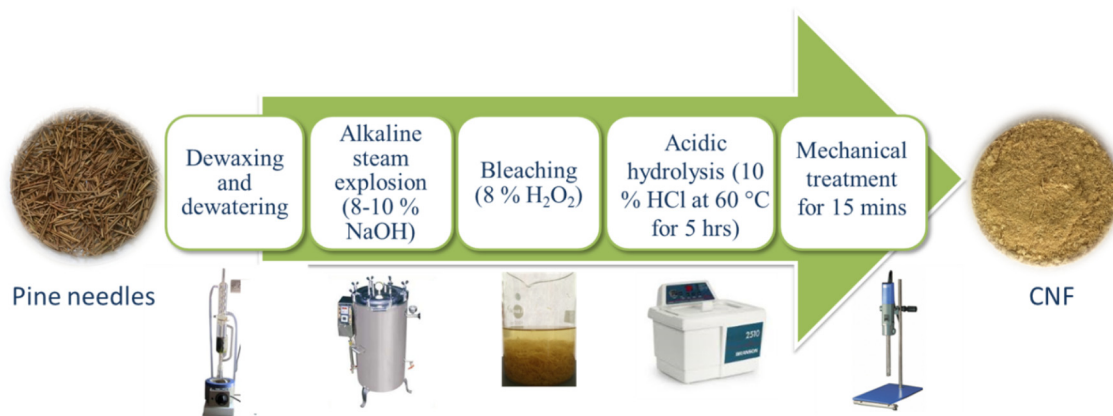
Pine needles were obtained from pine trees (Hamirpur, H.P.). They were thoroughly washed and dried before use to remove dust. Nickel nitrate (Ni(NO<sub>3</sub>)<sub>2</sub>·6H<sub>2</sub>O), ferric nitrate (Fe(NO<sub>3</sub>)<sub>3</sub>·9H<sub>2</sub>O), sodium borohydride (NaBH<sub>4</sub>), hydrogen peroxide (H<sub>2</sub>O<sub>2</sub>, 30% w/v) were procured from Fisher Scientific. Hydrochloric acid (HCl, 36%), absolute ethanol (99.9%) were obtained from Merck. 2-Nitrophenol (98%), 4-Nitrophenol (99%), 3-Nitrophenol, sodium hydroxide, tetraethyl orthosilicate (TEOS, Si(OC<sub>2</sub>H<sub>5</sub>)<sub>4</sub>) were supplied by AVRA synthesis. Remazol Black 5 (RB5) was obtained from Dyestar India Pvt. Ltd. All the chemicals used were of analytical grade.

### 2.2. Synthesis of nanocomposites

#### 2.2.1. Extraction of CNF from biowaste (pine needles)

CNF was extracted from pine needles using the procedure reported by Kaushik and Singh (2011). The extraction process consists of series of chemical treatment followed by mechanical treatment as shown in Scheme 1.

1. Dewaxing: The pine needles were extracted in soxhlet apparatus using benzene-ethanol mixture (2:1, v:v) at 50–60 °C for 5 h. The dewaxed samples were dried overnight in vacuum oven at 90 °C before use.
2. Delignification: Delignification was carried out in two steps:
  - (a) Alkali steam treatment: The dewaxed samples were soaked overnight in 2% NaOH solution followed by treatment with 8–10% NaOH solution in an autoclave at a temperature of 200 °C and at pressure around 20 lbs for 4 h. The sample was thoroughly washed with distilled water. Through this method, major quantity of lignin was removed.
  - (b) Bleaching treatment: The sample was then soaked in 8% H<sub>2</sub>O<sub>2</sub> solution (v/v) overnight to remove residual lignin and hemicellulose. The bleached pulp was washed with distilled water.
3. Ultrasonic treatment: The bleached pulp was treated with 10% HCl in an ultrasonicator at temperature of around 60 °C for 5 h. The fibres were washed till neutral pH and dried.



**Scheme 1** Extraction of CNF from pine needles.

4. High shear treatment: The fibres were suspended in water and mechanically treated using Fluko FA25 high shear homogenizer for 15–20 min to disintegrate the fibre agglomerates. The suspension was kept in an oven at 90 °C till dry resulting in formation of nanofibrils.

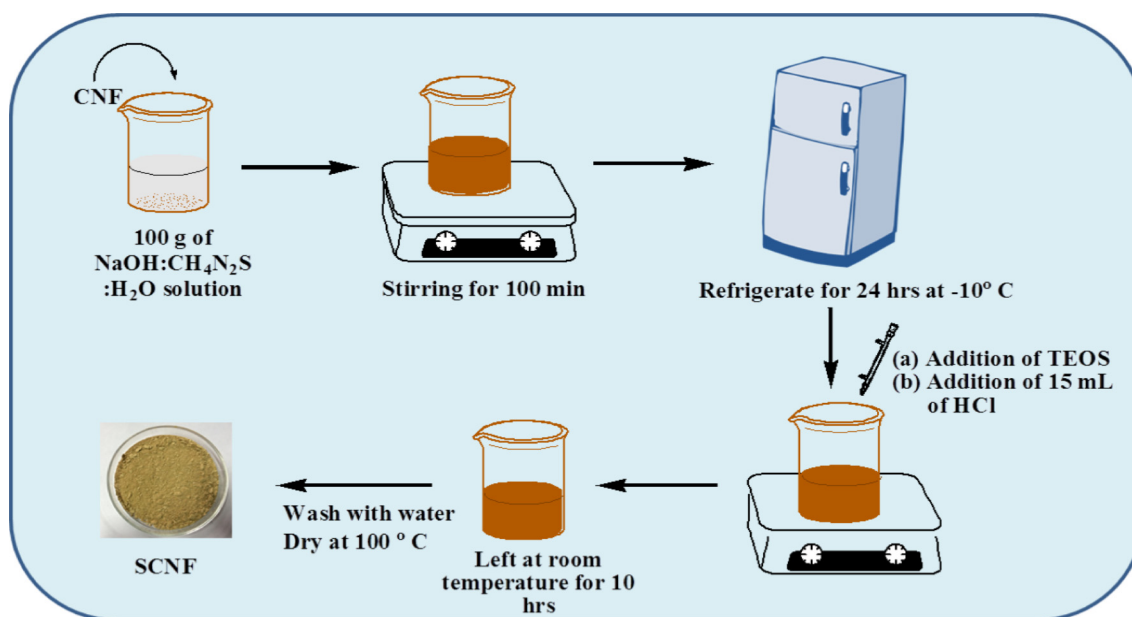
#### 2.2.2. Silanization of CNF (SCNF)

Silanization of CNF was carried out using the method as shown in [Scheme 2](#) ([Wang et al., 2016](#)). Firstly 100 g of aqueous solution (CH<sub>4</sub>N<sub>2</sub>S:NaOH:H<sub>2</sub>O) = 1:2.1:19.1 (w/w/w) with 4.5 g of CH<sub>4</sub>N<sub>2</sub>S was prepared. To this solution, 3 g of CNF was added and vigorously stirred for 100 min to form a homogeneous emulsion. The emulsion formed was refrigerated at –10 °C for 24 h to dissolve CNF and then thawed at room temperature to obtain cellulose solution. Afterwards to the obtained cellulose solution, required amount of TEOS was added followed by dropwise addition of 15 mL of 4 mol/L of HCl under magnetic stirring to obtain gel. The gel formed

was left at room temperature for 10 h and then washed and dried at 100 °C to obtain SCNF.

#### 2.2.3. Synthesis of CNF/SCNF-NiFe nanocomposites

For the synthesis of CNF-NiFe nanocomposites, CNF was added while synthesizing NiFe nanoparticles ([Srivastava et al., 2009](#)). In a typical synthesis, required amount of CNF were suspended in water and stirred in high shear homogeniser for 10–15 min to break the fibre agglomerates. Separately 0.291 g of Ni(NO<sub>3</sub>)<sub>2</sub>·6H<sub>2</sub>O and 0.808 g of Fe(NO<sub>3</sub>)<sub>3</sub>·9H<sub>2</sub>O were dissolved in minimum amount of water. The prepared salt solution was added dropwise to the cellulose solution. Then the pH of solution was adjusted to 7.5 by adding liquor ammonia followed by stirring for 2 h. Then the obtained solution was transferred to Teflon lined stainless steel autoclave and hydrothermally treated at 160 °C for 15 h. The product was filtered and washed with deionised water several times. The precipitates were dried at 70 °C for 10 h. Following the above procedure, series of cellulose-NiFe<sub>2</sub>O<sub>4</sub> nanocomposites



**Scheme 2** Silanization of CNF (SCNF).

were prepared with varying NiFe: CNF weight ratios (1:1.5, 1:2.5, 1:5). Following the same procedure, SCNF was added instead of CNF to synthesise SCNF-NiFe composite.

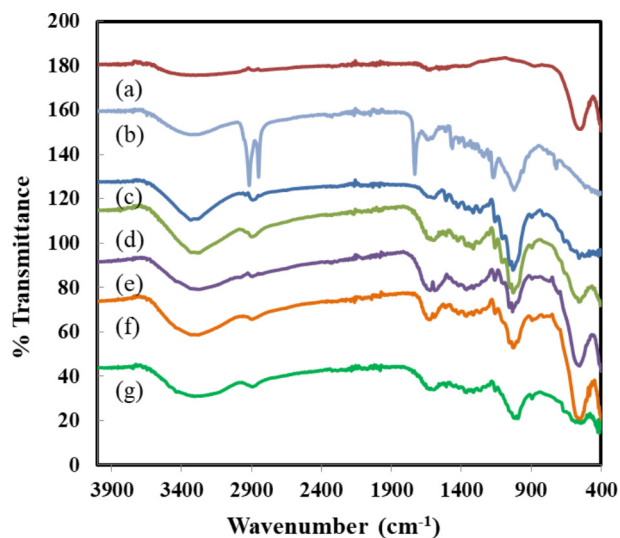


**Fig. 1** FT-IR spectra of (a) NiFe, (b) raw material (pine needles), (c) CNF, (d) CNF-NiFe (5:1), (e) CNF-NiFe (2.5:1), (f) CNF-NiFe (1.5:1) and (g) SCNF-NiFe (2.5:1).

### 2.3. Physical measurements

The chemical structures of synthesized samples were characterized on iS50-FTIR (Model No. AUP1200343) spectrophotometer. The Fourier Transform Infrared (FT-IR) spectra were collected in the range of 4000–400  $\text{cm}^{-1}$  with a resolution of 1  $\text{cm}^{-1}$ . The crystal structures were studied from Powder X-ray diffraction (XRD) patterns which were recorded on Panalytical's X'Pert Pro diffractometer in the  $2\theta$  range of 10–80° with a scan rate of 4°  $\text{min}^{-1}$ . High Resolution Transmission Electron Microscopy (HR-TEM) analysis was done using FEI Tecnai (G2 F20) operating at 200 keV. Magnetic properties of the samples were characterized using Vibrating Sample Magnetometer (VSM) (155 PAR) by measuring the applied field dependence of magnetization in the magnetic field range of –10,000 Oe to 10,000 Oe at room temperature. The specific surface area of the samples was determined by  $\text{N}_2$  sorption at 77 K using Brunauer–Emmett–Teller (BET) surface analyser ((11-2370) Gemini, Micromeritics, USA). The optical absorption measurements were carried out using UV–visible spectrophotometer (JASCO-V750).

### 2.4. Catalytic procedures

To establish the utility of the synthesized samples as catalyst, the catalytic efficiency of all the synthesized nanocomposites

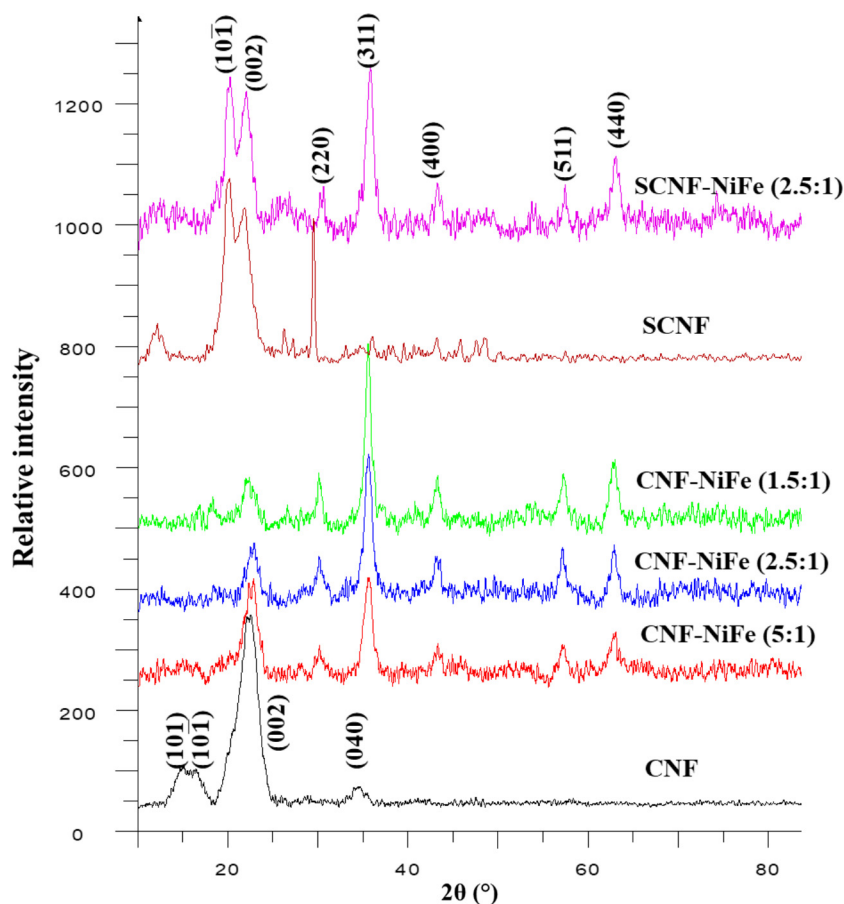


**Fig. 2** Powder X-ray diffractograms of cellulose nanofibres (CNF), silanized cellulose (SCNF) and their composites with  $\text{NiFe}_2\text{O}_4$  (NiFe).

has been estimated for both the oxidation and reduction reactions. The photo Fenton degradation of dye and reduction of nitrophenols were chosen as model reactions as visible color change indicates the completion of reaction.

#### 2.4.1. Photo Fenton degradation of dyes

Remazol Black 5 (RB5) was chosen as a probe molecule to evaluate the photo-catalytic efficiency of the synthesized samples. The entire experiments were conducted under Xe lamp as a light source at room temperature. In a typical experiment, desired amount of catalyst was added to 100 mL of RB5 dye solution (50 mg/L). The pH of solution was adjusted to 2.5 by adding sulphuric acid followed by stirring in dark for 30 min to acquire adsorption-desorption equilibrium. Prior to irradiation, 0.1 mL of H<sub>2</sub>O<sub>2</sub> (30% w/v) was added to the solution and aliquots of sample were withdrawn at regular intervals. The reaction progress was monitored using UV-visible spectrophotometer.

#### 2.4.2. Reduction of nitrophenols

Nitrophenols were chosen as model compounds for reduction reaction as they are the major organic pollutants and can be converted to useful amines by using NaBH<sub>4</sub> as a reducing agent. In a typical experiment, aqueous solution of nitrophenol was taken and 50 equivalents of NaBH<sub>4</sub> were added followed by the addition of 50 mg of synthesized catalyst. At desired intervals, aliquots from the reaction mixture were withdrawn and subsequently diluted and their absorbance was recorded

using UV-visible spectrophotometer to monitor the progress of reaction. The dark yellow color of nitrophenols diminishes, demonstrating the conversion of nitrophenols to nitroamines.

### 3. Results and discussions

#### 3.1. FT-IR studies

FT-IR spectroscopy is one of the most important analytical tools used to characterize a compound structurally. This technique is used to acquire information about various functional groups present in the compound. So using FT-IR spectroscopy, successful formation of CNF and its nanocomposites is confirmed. The FT-IR spectra of pine needles, NiFe, CNF and all the synthesized nanocomposites with varying CNF:NiFe ratio was recorded and the results are presented in Fig. 1. In the FT-IR spectra of raw material i.e. pine needles, the bands around 1730 cm<sup>-1</sup> and 1510 cm<sup>-1</sup> are mainly due to the stretching vibrations in lignin and hemicellulose. These bands disappear in the spectra of CNF clearly indicating the removal of most hemicellulose and lignin from CNF (Xiao et al., 2015). The absorption band in the spectra of CNF at around 3300 cm<sup>-1</sup> is assigned to the stretching vibrations of -OH groups of the cellulose. Absorption band in the range of 2850–2900 cm<sup>-1</sup> and 1430–1480 cm<sup>-1</sup> is attributed to the symmetrical -CH<sub>2</sub> stretching vibration and symmetrical -CH<sub>2</sub> bending vibrations respectively (Nelson and O'Connor, 1964). Absorption peak at around 1600 cm<sup>-1</sup> is

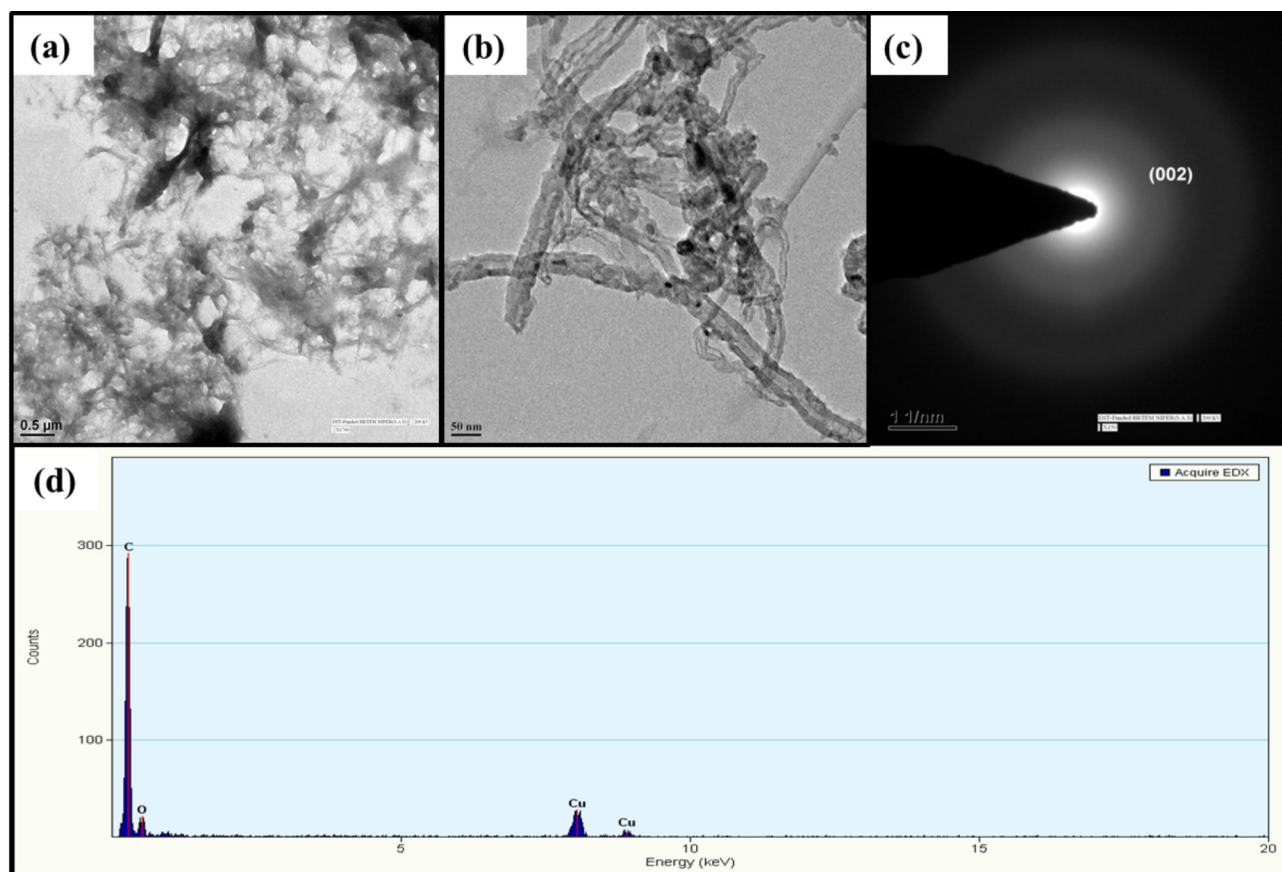


Fig. 3 TEM images of CNF (a) and (b) at low resolution, (c) SAED pattern and (d) EDX pattern.

**Table 1** Powder X-ray diffraction parameters for the synthesized samples.

Sample	Lattice parametera (Å)	Average crystallite size d (nm)	
		CNF	NiFe
CNF	–	3.3	–
CNF-NiFe (5:1)	8.352	4.7	7.3
CNF-NiFe (2.5:1)	8.347	4.8	8.7
CNF-NiFe (1.5:1)	8.347	5.5	11.4
SCNF-NiFe (2.5:1)	8.346	7.3	10.1

due to the aromatic C=C stretching vibrations suggesting the presence of aromatic ring structures (Pang et al., 2014). The band attributed to C—O stretching vibration of cellulose appears at around  $1030\text{ cm}^{-1}$ . On comparing the FT-IR spectra of CNF and the nanocomposites, it can be clearly seen that in the spectra of nanocomposites, the band corresponding to —OH group of cellulose shifted to lower wave number with relatively decreased intensity. This can be attributed to the fact that surface hydroxyl groups of cellulose interacts with the surface of magnetic nanoparticles (Marková et al., 2012). Also a new band is observed in the range of  $530\text{--}560\text{ cm}^{-1}$  in the spectra of nanocomposites which can be ascribed to the Ni—O stretching vibration present in the tetrahedral site of NiFe lattice (Priyadharsini et al., 2009). Based on the FTIR analysis, the attachment of NiFe nanoparticles on the surface of CNF

has been confirmed. Besides this, in case of SCNF:NiFe, the band due to Si—O—Si and Si—O—C could not be assigned due to overlapping of Si—O and C—O stretching in the region of  $1030\text{--}1150\text{ cm}^{-1}$  (Wang et al., 2016). The band due to OH stretching is broader and weaker as compared to other composites due to the hydrogen bonding between CNF and silanol groups.

### 3.2. Powder XRD studies

Powder XRD technique is a rapid and versatile technique used for the evaluation of crystallinity and phase purity of crystalline compounds. Powder XRD studies were carried out to get information about the crystalline phases present in cellulose and the nanocomposites and for the confirmation of presence of both CNF and NiFe in the composites. Fig. 2 shows the XRD pattern of CNF and its nanocomposites with NiFe. The XRD pattern of CNF shows diffraction peaks around  $2\theta = 14.92^\circ$  (1 0 1),  $16.49^\circ$  ( $10\bar{1}$ ),  $22.5^\circ$  (0 0 2),  $34.36^\circ$  (0 4 0) which represents the typical cellulose I structure (Park et al., 2010) (JCPDS card No. (00-050-2241). Once CNF is regenerated during the silanization, the XRD pattern of SCNF and SCNF-NiFe exhibits peaks with diffraction angles around  $2\theta = 19.89^\circ$  ( $10\bar{1}$ ) and  $21.86^\circ$  (0 0 2) which are consistent with cellulose II structure. This correlates with the fact that the cellulose changes its crystal structure from I to II upon regeneration (Sun et al., 2014; Kuo and Lee, 2009). In the XRD pattern of nanocomposites, besides the typical peak of cellulose at

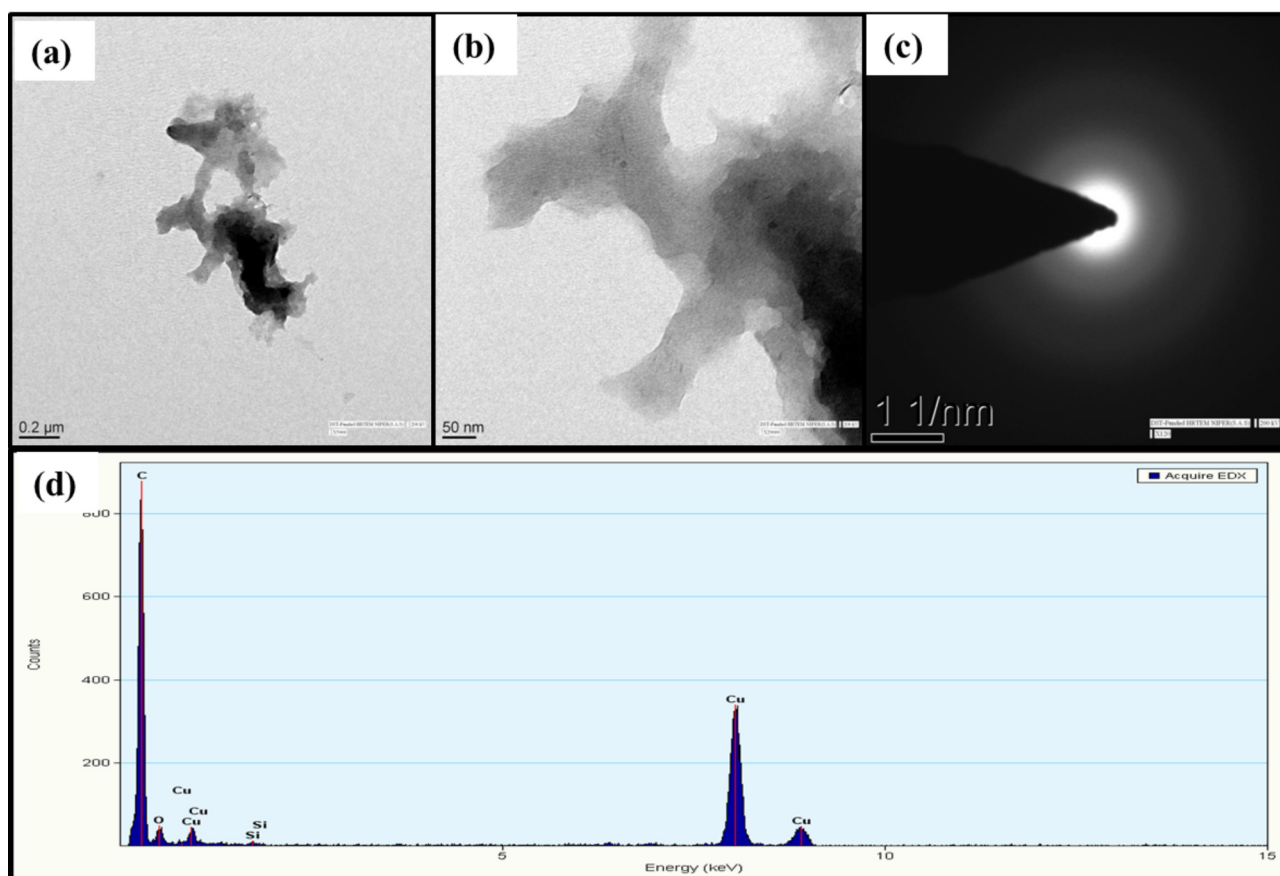


**Fig. 4** TEM images of SCNF (a) and (b) at low resolution, (c) SAED pattern and (d) EDX pattern.

$2\theta = 22.5^\circ$  (0 0 2), there are some other diffraction peaks at  $2\theta = 30.20^\circ$ ,  $35.75^\circ$ ,  $43.37^\circ$ ,  $57.55^\circ$ ,  $62.22^\circ$  which corresponds to (2 2 0), (3 1 1), (4 0 0), (5 1 1) and (4 4 0) planes of NiFe, respectively. All these peaks match well with the standard pattern of NiFe (JCPDS card no. 10-0325). As the ratio of CNF: NiFe is decreasing, the peaks corresponding to NiFe become more sharp and intense while that corresponding to CNF, decrease in intensity as shown in the Fig. 3. The XRD results indicate that the synthesized nanocomposites are composed of both cellulose and NiFe nanoparticles. The crystallite size was calculated from the line broadening of most intense (0 0 2) and (3 1 1) peak of CNF and NiFe, respectively using Debye Scherrer equation (Hossain and Rahman, 2011). The Le Bail refinement method was used to calculate lattice parameters. The values of lattice parameter were found to be in range of 8.347–8.352. The values of crystallite size and lattice parameters of CNF and its composites with NiFe are tabulated in Table 1.

### 3.3. HR-TEM studies

HR-TEM technique is employed for the structural and morphological characterization of the samples. SAED and EDS techniques are used in association with the HR-TEM technique. SAED pattern confirms the crystalline nature and EDS allows the measurement of elemental composition of the samples. To prepare the samples for HR-TEM studies, CNF and the synthesized nanocomposites were first dispersed

in absolute ethanol using sonication for 3–4 h. The samples were then coated on carbon coated Cu grids and TEM micrographs were recorded. Fig. 3(a) and (b) shows the low resolution TEM images of CNF. Fig. 3(a) reveals that the cellulose exists in the form of an interconnected mesh type network. On further magnification to 50 nm (Fig. 3(b)), it was observed that the mesh type network consists of entangled nanofibres. The SAED image (Fig. 3(c)) shows diffraction ring corresponding to (0 0 2) plane of cellulose. The EDX spectrum (Fig. 3(d)) shows the presence of only carbon and oxygen elements indicating high purity of the sample. Fig. 4(a) and (b) shows the low resolution TEM images of SCNF and (c) shows the SAED pattern of SCNF. The EDX pattern (d) shows an additional peak corresponding to Si, confirming the successful silanization of CNF. Figs. 5–8 ((a) and (b)) shows the low resolution TEM images of the synthesized nanocomposites. The TEM observation reveals good dispersion of NiFe nanoparticles into cellulose matrix which further confirms that NiFe nanoparticles are tightly anchored on the surface of CNF. Such strong combination contributes to prevent the agglomeration of magnetic nanoparticles thereby increasing their surface energy and hence catalytic efficiency. The HR-TEM images (Figs. 5–8(c)) depict the visible lattice fringes with interplanar spacing of 0.48 nm, 0.29 nm, 0.25 nm and 0.24 nm which corresponds to (1 1 1), (2 2 0), (3 1 1) and (2 2 2) planes, respectively of the cubic phase of NiFe confirming the presence of NiFe nanoparticles in the composite. The SAED pattern (Figs. 5–8(d)) of all nanocomposites displays concentric dark

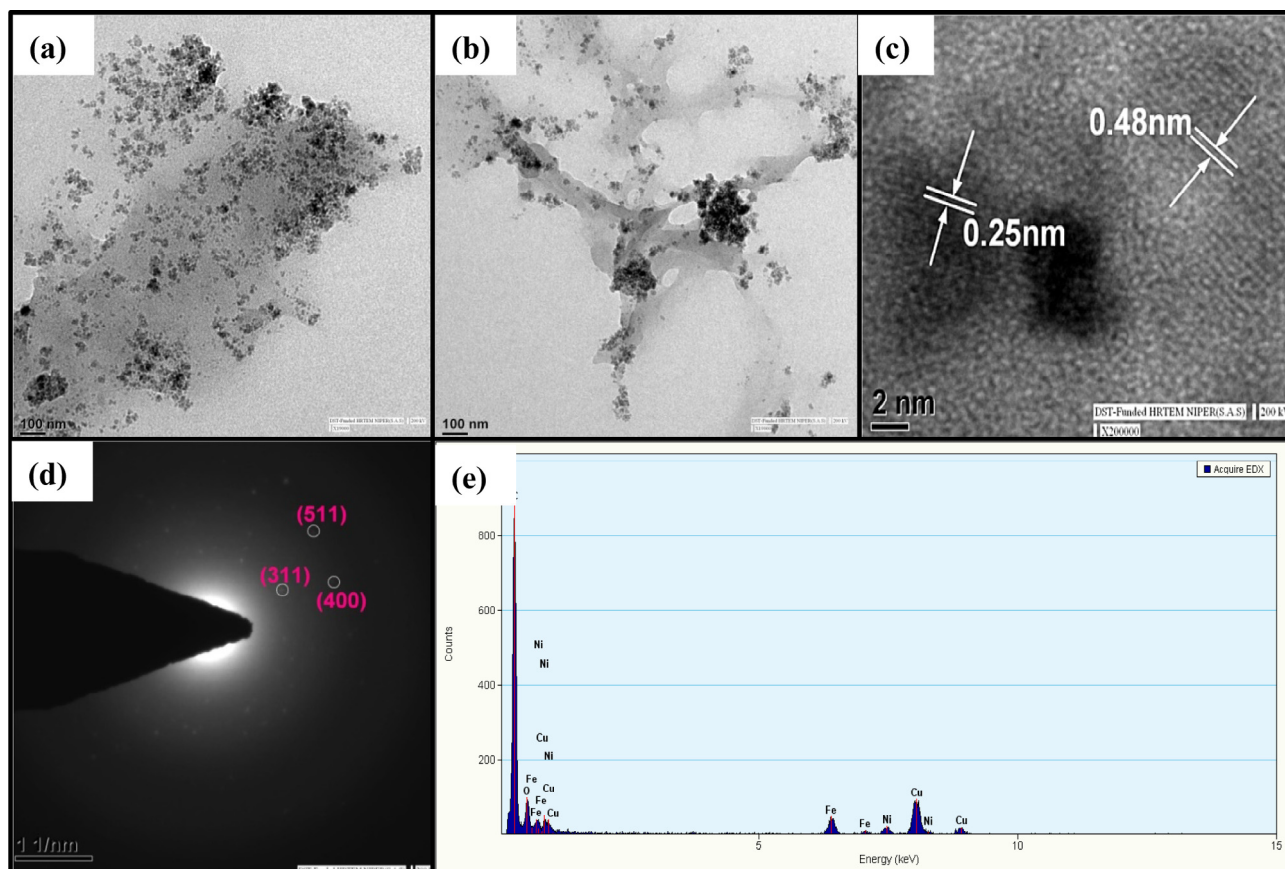
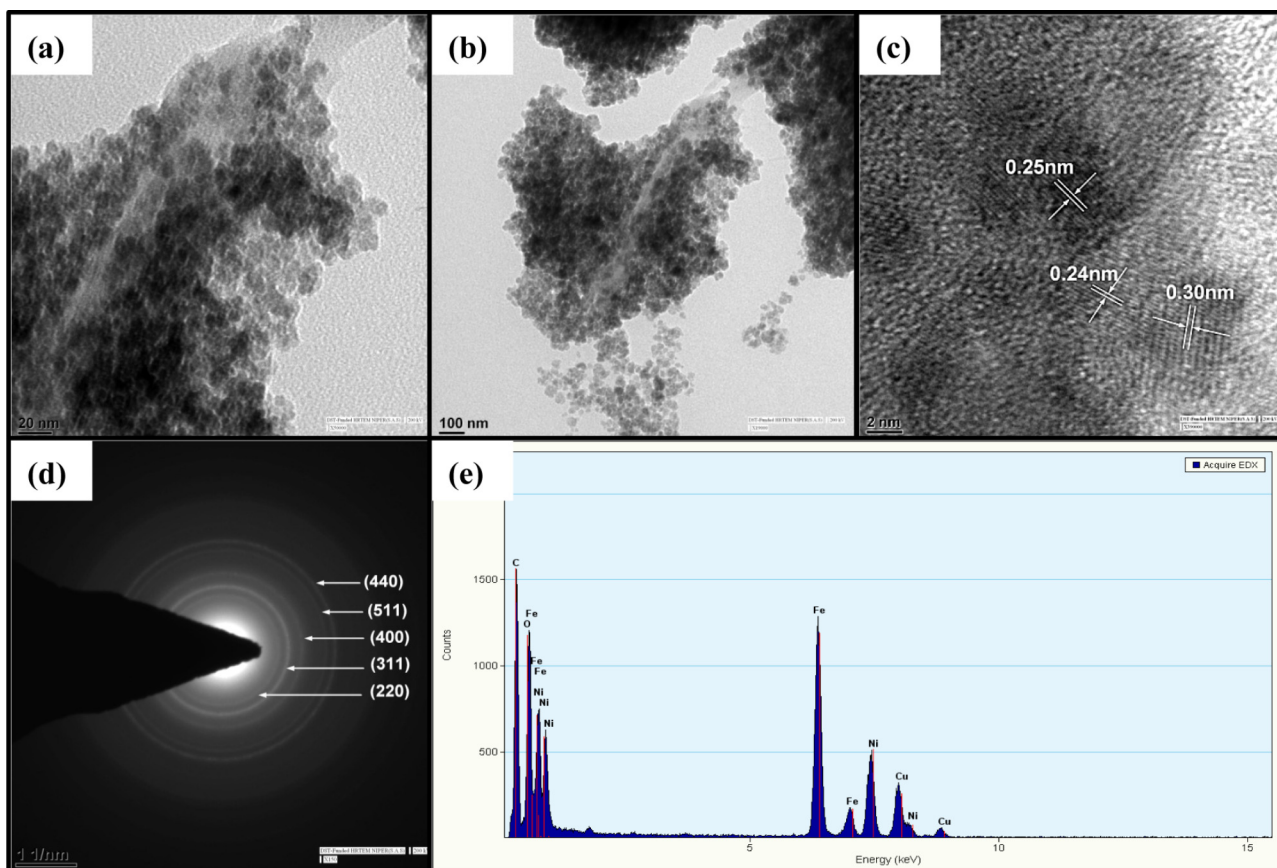


Fig. 5 TEM images of CNF-NiFe (5:1) (a) and (b) at low resolution, (c) at high resolution, (d) SAED pattern and (e) EDX pattern.



**Fig. 6** TEM images of CNF-NiFe (2.5:1) (a) and (b) at low resolution, (c) at high resolution, (d) SAED pattern and (e) EDX pattern.

and bright rings indicating the highly crystalline nature of the samples. These concentric rings correspond to lattice planes that can be indexed to standard NiFe diffraction data. The EDX patterns (Figs. 5–8(e)) of the nanocomposites show the presence of Fe, Ni, C and O elements corresponding to NiFe and CNF while the EDX pattern of SCNF: NiFe (Fig. 8(e)) shows an additional peak corresponding to Si due to formation of composite with silanized cellulose (SCNF). No peak corresponding to any other element was found, indicating purity of the sample. Peaks corresponding to Cu were observed due to the use of Cu grids for analysis.

### 3.4. Magnetic studies

Cellulose is non-magnetic in nature. So to fabricate magnetically retrievable cellulose based nanocomposites, NiFe was added to the cellulose matrix. Hence magnetic studies were conducted to confirm the magnetic nature of the synthesized nanocomposites. Hysteresis loops of the synthesized nanocomposites and NiFe were recorded at room temperature with an applied magnetic field of  $\pm 10$  kOe using Vibrating Sample Magnetometer (VSM). The values of saturation magnetization ( $M_s$ ), remanence ( $M_r$ ), coercivity ( $H_c$ ) and squareness ratio of all the samples were calculated from hysteresis loop shown in Fig. 9 and values are tabulated in Table 2. The  $M_s$  value for NiFe was found to be 46.39 emu/g. The  $M_s$  values for all the nanocomposites were found to be lower than pristine NiFe due to presence of non-magnetic cellulose in the nanocomposites.

On comparing the  $M_s$  values for the nanocomposites, it was observed that CNF-NiFe (1.5:1) shows the highest saturation magnetization. As it is well known that particle size has significant effect on the saturation magnetization, larger the particle size, greater is the saturation magnetization (Dhiman et al., 2016). The larger crystallite size of NiFe in CNF-NiFe (1.5:1) as depicted in the XRD data shown, confirms the reason for its higher saturation magnetization. The remanence values were found to decrease while coercivity values increased for the synthesized nanocomposites as compared to bare NiFe nanoparticles. Though the saturation magnetization values are lower for the nanocomposites, still the nanocomposites exhibit strong magnetic responsiveness and can be easily recovered by the use of external magnet from the reaction mixture.

### 3.5. Surface area studies

In the present investigation, the synthesized nanocomposites have been evaluated for their catalytic activity. It is well known that catalysis is a surface phenomenon. Greater surface area means more catalytic sites are available on the surface of catalyst for a reaction to occur. Therefore, more the surface area more would be the catalytic activity. So, surface area is a very crucial factor to determine the catalytic efficiency of a material. Hence surface area studies were carried out using single point BET analyser. The samples were degassed at 100 °C for 1 h prior to nitrogen adsorption. The BET adsorption isotherms were plotted between  $1/[Q\{(P_0/P) - 1\}]$  vs.  $P/P_0$  and specific

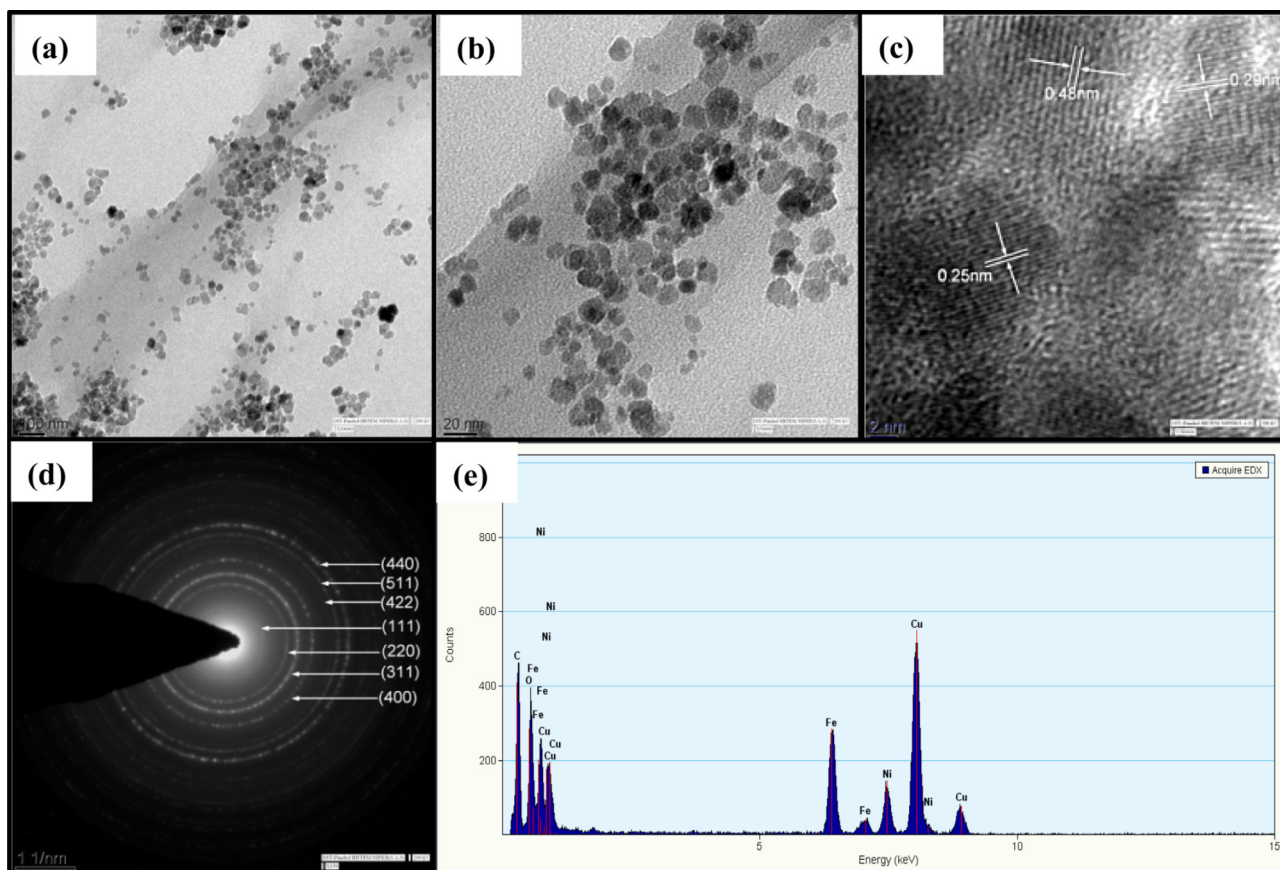


**Fig. 7** TEM images of CNF-NiFe (1.5:1) (a) and (b) at low resolution, (c) at high resolution, (d) SAED pattern and (e) EDX pattern.

surface area values were calculated from the plots. The specific surface area values were found to be 30.279 m<sup>2</sup> g<sup>-1</sup> for CNF, 590.096 m<sup>2</sup> g<sup>-1</sup> for CNF-NiFe (2.5:1) and 634.51 m<sup>2</sup> g<sup>-1</sup> for SCNF-NiFe (2.5:1). As there is direct relation between surface area and catalytic efficiency, so the catalytic activity is also intended to follow the same order as the surface area studies.

### 3.6. Catalytic studies

After the successful synthesis and characterization of nanocomposites, the next step was to evaluate the catalytic performance of the synthesized samples. As magnetic studies clearly indicates that all the synthesized nanocomposites are magnetic in nature and can be easily recovered using external magnet, so taking advantage of this property, the main aim of this work was to develop cellulose based nanocomposites which would act as magnetically retrievable green catalysts for the mitigation of organic pollutants. Dyes and nitrophenols are among the major organic pollutants, so their degradation was chosen as a model reaction to estimate their catalytic efficiency.

#### 3.6.1. Photo-Fenton degradation of toxic dye

**3.6.1.1. Control experiments.** The degradation of RB5 was carried out to access the photocatalytic efficiency of the synthesized nanocomposites. Various factors affect the degradation process. So firstly, control experiments were performed in

order to understand the effect of different components on the Fenton degradation process. Reactions were carried out to study the individual effect of H<sub>2</sub>O<sub>2</sub>, catalyst and light source. **Fig. 10** shows a set of control experiments performed (a) dye + H<sub>2</sub>O<sub>2</sub> (b) with dye + light + NiFe, (c) dye + H<sub>2</sub>O<sub>2</sub> + NiFe, (d) dye + light + H<sub>2</sub>O<sub>2</sub> + ferrite. The results indicated that almost negligible degradation was observed when only H<sub>2</sub>O<sub>2</sub> was added (a). This could be attributed to the fact that peroxide has low oxidation potential as compared to hydroxyl radical. As is clear from the figure, very less degradation was achieved upon the addition of only ferrite in the presence of light (b). The degradation rate was slightly enhanced when ferrite and H<sub>2</sub>O<sub>2</sub> were used in absence of light (c). However, a sharp increase was observed when H<sub>2</sub>O<sub>2</sub> and ferrite were used in the presence of light suggesting that all the three components H<sub>2</sub>O<sub>2</sub>, light source and catalyst are mandatory for the degradation process to occur at fast rate. In presence of 0.50 g/L of CNF as catalyst, only 10% dye degraded in 120 min.

**3.6.1.2. Effect of catalyst loading on degradation of RB5 by synthesized nanocomposites.** The photo Fenton degradation of RB5 was studied using NiFe, CNF-NiFe (5:1), CNF-NiFe (2.5:1), CNF-NiFe (1.5:1) and SCNF-NiFe (2.5:1). The typical time dependant UV-visible spectrum for the photocatalytic degradation of RB5 using CNF-NiFe (2.5:1) as catalyst is shown in **Fig. 11**.

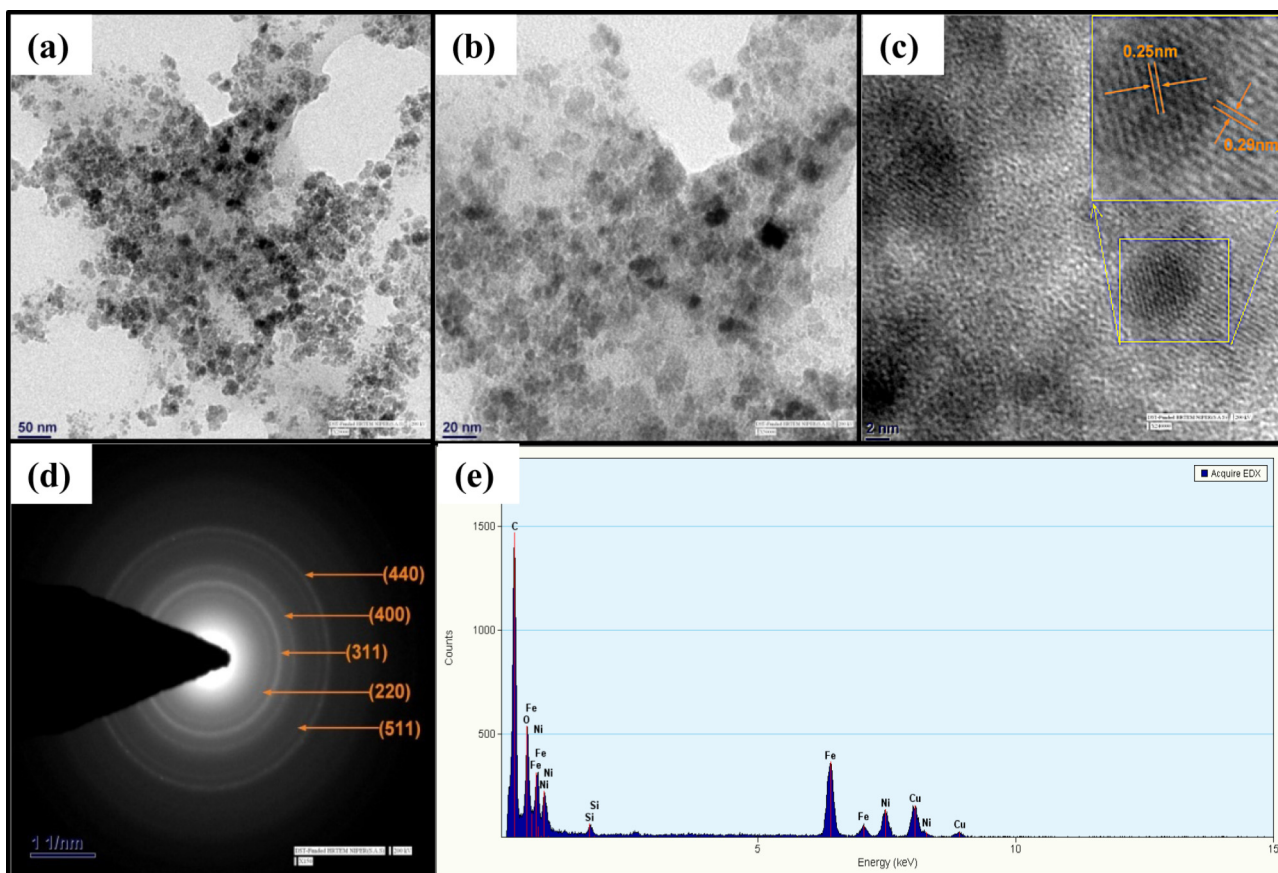


**Fig. 8** TEM images of SCNF-NiFe (2.5:1) (a) and (b) at low resolution, (c) at high resolution, (d) SAED pattern and (e) EDX pattern.

As catalysis is a surface phenomenon, so the number of catalytic sites available on the surface play a crucial role in deciding the proficiency of a catalyst. Hence the effect of catalyst loading on the degradation efficiency was evaluated by varying the catalytic amount from 0.25 g/L to 0.75 g/L. The results demonstrated that there is increase in the reaction rate with initial increase in catalyst from 0.25 g/L to 0.50 g/L. This increase is due to the increase in number of catalytic sites present on the surface of catalyst. However, with further increase in the amount of catalyst, there is decrease in the rate, which can be attributed to increase in scattering of incident light leading to decrease in penetration of light through the solution (Kaur et al., 2016). The highest degradation efficiency was achieved when the catalyst loading was 0.50 g/L.

**3.6.1.3. UV-visible spectroscopy.** The UV-vis absorption maxima for RB5 dye is observed at 597 nm (Sharma and Singhal, 2015). As the reaction proceeded, the absorption band gradually decreased in intensity and the complete disappearance of this band indicated the complete degradation of dye. The absorbance vs. time graphs for all the synthesized samples at varying catalyst loading are shown in Fig. 12. The percentage of dye degraded at any time was calculated using Eq. (1).

$$\% \text{ degradation} = \frac{A_0 - A_t}{A_0} \times 100 \quad (1)$$

where  $A_0$  is initial absorption intensity of dye and  $A_t$  is absorption intensity of dye at time  $t$ .

An appreciable difference in the percentage degradation was observed when we compared the degradation process using pristine NiFe nanoparticles and the synthesized nanocomposites as catalyst. 73% degradation was observed with NiFe as a catalyst while almost 98% degradation took place on using SCNF-NiFe as a catalyst. Similarly all the other synthesized nanocomposites depicted higher degradation rates and hence better photocatalytic efficiency as compared to pristine NiFe nanoparticles.

**3.6.1.4. Chemical kinetics.** The degradation reaction was observed to follow pseudo first order kinetics. The rate constant can be calculated using the slope of rate law equation (2).

$$\ln \frac{A_0}{A_t} = kt \quad (2)$$

where  $k$  is the rate constant.  $\ln A_0/A_t$  vs. time graphs were plotted and rate constant values were calculated from the slope of these plots. The plots of  $\ln A_0/A_t$  vs. time for all the synthesized samples at varying catalyst loading are shown in Fig. 13. The corresponding rate constant value for all the plots are given in Table 3.

The rate constant value for degradation using NiFe was  $0.0122 \text{ min}^{-1}$  while for CNF-NiFe (2.5:1), it was  $0.0343 \text{ min}^{-1}$  (catalyst loading 0.50 g/L for both). From the values of rate constant, it is evident that CNF-NiFe (2.5:1) is a highly efficient catalyst in the photo Fenton degradation of RB5 out of the three nanocomposites with varying CNF-NiFe

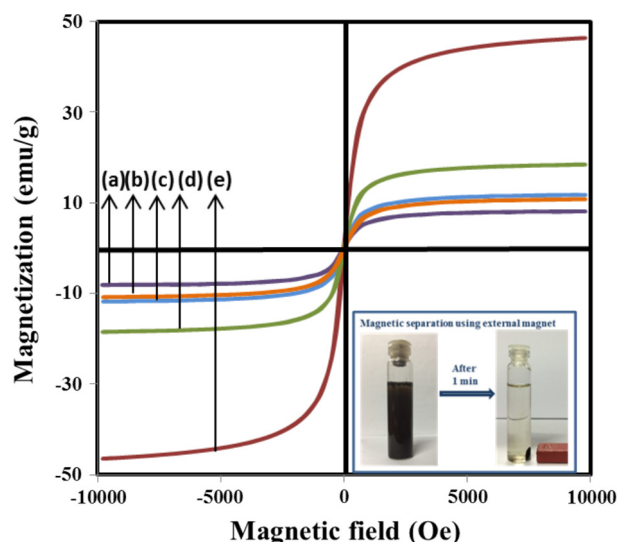


**Fig. 9** Room temperature hysteresis loops for (a) CNF-NiFe (5:1), (b) SCNF-NiFe (2.5:1), (c) CNF-NiFe (2.5:1), (d) CNF-NiFe (1.5:1) and (e) NiFe.

synthesized. This could be attributed to the synergistic effect between CNF-NiFe at this composition. Further silanization of CNF was done and the nanocomposite was synthesized using the best composition of CNF: NiFe i.e. 2.5:1. Silanization of CNF further augmented the catalytic efficiency of the synthesized nanocomposite, SCNF-NiFe (2.5:1) as is demonstrated by the plots of  $\ln A_0/A_t$  vs. time and the rate constant values. This may be due to the fact that silica derivatives of cellulose improve the thermal stability of cellulose and its affinity towards special substrates (Taha et al., 2012). The results obtained can also be explained on the basis of surface area. It is well known that catalysis is a surface phenomenon and surface area and catalysis are related to each other. Greater the surface area greater will be the catalytic efficiency. Hence the obtained sequence of surface area analysis coincides with the sequence of obtained photocatalytic efficiency. The surface area value obtained for SCNF-NiFe (2.5:1) was highest and so is its catalytic efficiency. The photocatalytic activity of the synthesized samples follows the order SCNF-NiFe (2.5:1) > CNF-NiFe (2.5:1) > CNF-NiFe (5:1) > CNF-NiFe (1.5:1) > NiFe.

### 3.6.2. Reduction of nitrophenols

The reduction of nitrophenols was studied in aqueous medium in presence of NaBH<sub>4</sub> as a reducing agent and synthesized nanocomposites and NiFe as catalyst. Control experiments revealed that the presence of both NaBH<sub>4</sub> and catalyst are

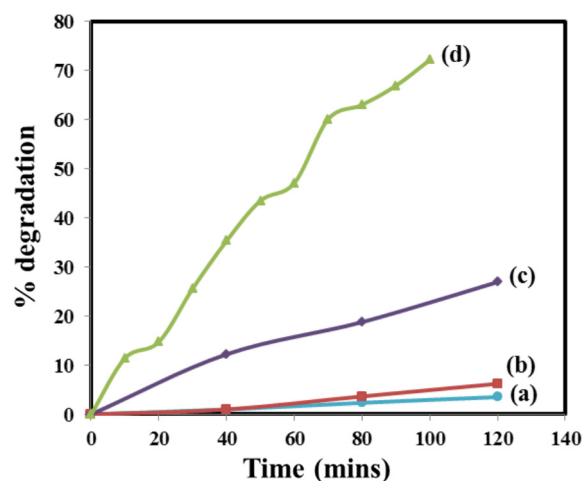


**Fig. 10** Control experiments for the photocatalytic degradation of RB5 using NiFe as a catalyst where conditions are (a) Dye + H<sub>2</sub>O<sub>2</sub>, (b) Dye + light + ferrite, (c) Dye + light + H<sub>2</sub>O<sub>2</sub> and (d) Dye + light + H<sub>2</sub>O<sub>2</sub> + Ferrite.

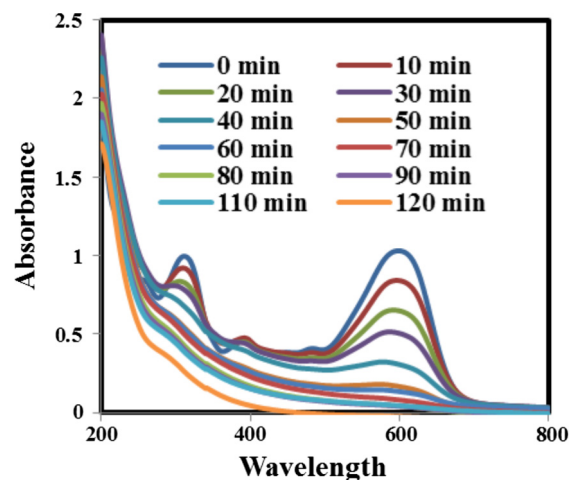


**Fig. 11** Typical time dependant UV-visible spectra for photocatalytic degradation of RB5 using CNF-NiFe (2.5:1) (50 mg) as catalyst.

mandatory for reduction reaction to occur. In the present investigation, reduction reactions were performed using 50 equivalents of NaBH<sub>4</sub> and 50 mg of catalyst. The reduction of 2-nitrophenol (2-NP), 3-nitrophenol (3-NP) and 4-nitrophenol (4-NP) has been performed to evaluate the catalytic performance of the synthesized nanocomposites.

**Table 2** Values of saturation magnetization ( $M_s$ ), remanence ( $M_r$ ), coercivity ( $H_c$ ) and squareness ratio for the synthesized samples.

Sample	Saturation magnetization ( $M_s$ ) (emu/g)	Remanence ( $M_r$ ) (emu/g)	Coercivity ( $H_c$ ) (Oe)	Squareness ratio ( $M_r/M_s$ ) * 10 <sup>-1</sup>
NiFe	46.4	0.8	14.5	0.17
CNF-NiFe (5:1)	8.1	0.2	21.5	0.24
CNF-NiFe (2.5:1)	11.8	0.34	22.0	0.28
CNF-NiFe (1.5:1)	18.5	0.33	14.5	0.18
SCNF-NiFe (2.5:1)	10.8	0.23	17.3	0.21

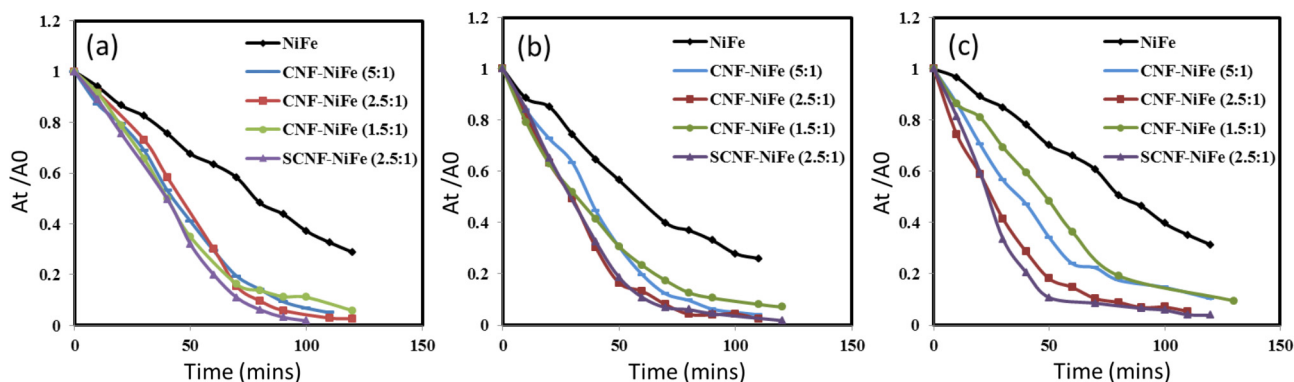


**Fig. 12**  $A_t/A_0$  vs. time graphs for NiFe and the synthesized nanocomposites with varying catalyst loading (a) 0.25 g/L, (b) 0.50 g/L and (c) 0.75 g/L for the photocatalytic degradation of RB5.

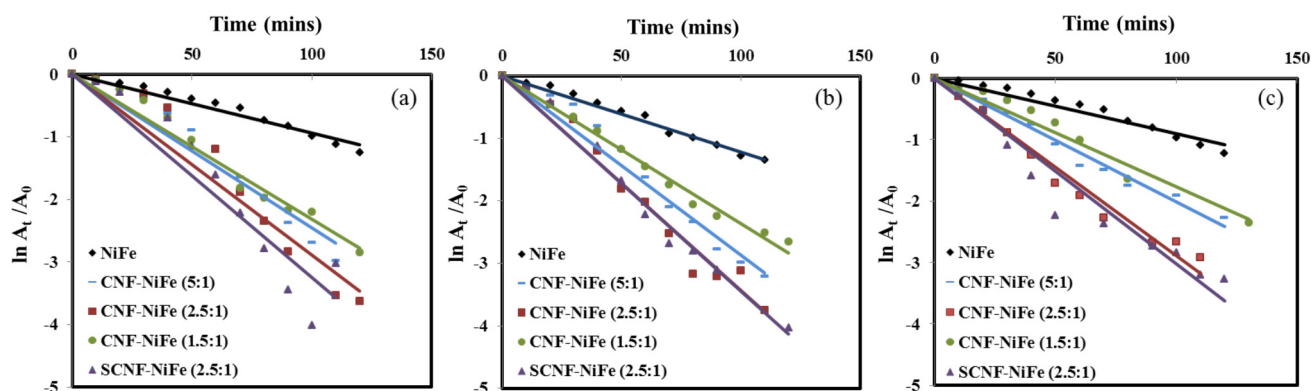


**Fig. 13**  $\ln A_t/A_0$  vs. time graphs for NiFe and the synthesized nanocomposites with varying catalyst loading (a) 0.25 g/L, (b) 0.50 g/L and (c) 0.75 g/L for the photocatalytic degradation of RB5.

**3.6.2.1. UV-visible spectroscopy.** UV-visible spectroscopy was used to monitor the reaction progress. The absorption maxima for 2-, 3- and 4- NP are observed at 350, 325 and 317 nm respectively in the UV-vis spectrum (Goyal et al., 2016). The typical UV-vis spectra for all the three nitrophenols using CNF-NiFe (2.5:1) are shown in Fig. 14. The absorbance vs. time plots for all the synthesized nanocomposites for the reduction of three nitrophenols are shown in Fig. 15. The results clearly indicates that significant enhancement in the reduction reaction was observed when pristine NiFe nanoparticles were supported on CNF to fabricate magnetically retrievable cellulose based nanocomposites.

**3.6.2.2. Chemical kinetics.** As  $\text{NaBH}_4$  is used in excess, the reduction reaction was considered to follow pseudo first order kinetics. The rate constant for the pseudo first order reaction can be calculated from integrated first order rate law equation. The plots of  $\ln A_0/A_t$  vs. time for all the synthesized nanocomposites for the reduction of 2-, 3-, 4- NP are shown in Fig. 16.

The apparent rate constant values are calculated from the slope of plots of  $\ln A_0/A_t$  vs. time and are given in Table 4. The rate constant values for reduction reaction using NiFe as catalyst were found to be  $0.136 \text{ min}^{-1}$  for 2-NP,

**Table 3** Rate constant values for the photocatalytic degradation of RB5 by NiFe and synthesized nanocomposites at varied catalyst loading.

Sample	Catalyst loading (g/l)	Rate constant ( $k \times 10^{-2}$ ) ( $\text{min}^{-1}$ )
NiFe	0.25	0.94
	0.50	1.22
	0.75	0.91
CNF-NiFe (5:1)	0.25	2.46
	0.50	2.86
	0.75	2.02
CNF-NiFe (2.5:1)	0.25	2.88
	0.50	3.43
	0.75	2.89
CNF-NiFe (1.5:1)	0.25	2.32
	0.50	2.36
	0.75	1.77
SCNF-NiFe (2.5:1)	0.25	3.24
	0.50	3.45
	0.75	3.02

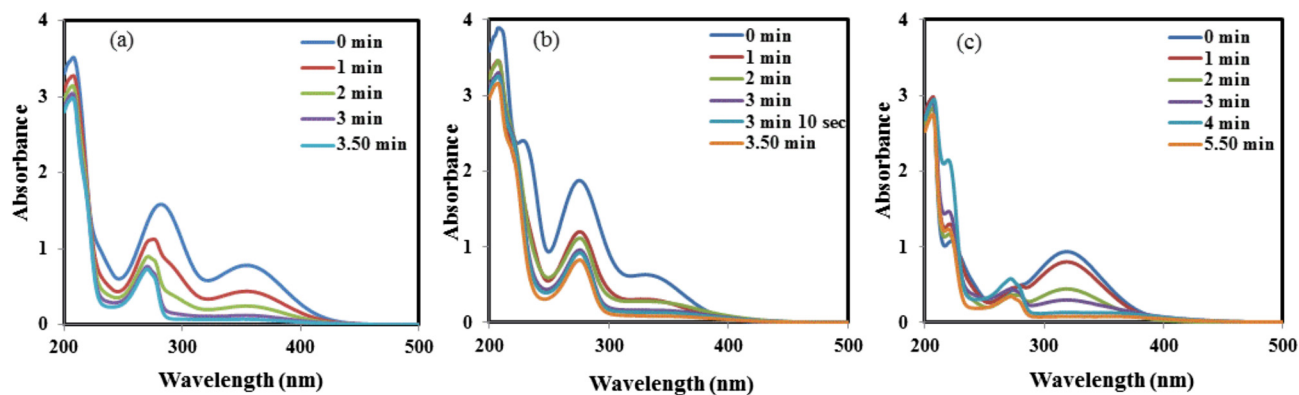


**Fig. 14** Typical time dependant UV-visible spectra for the reduction of (a) 2-NP, (b) 3-NP and (c) 4-NP in the presence of CNF-NiFe (2.5:1) as a catalyst.

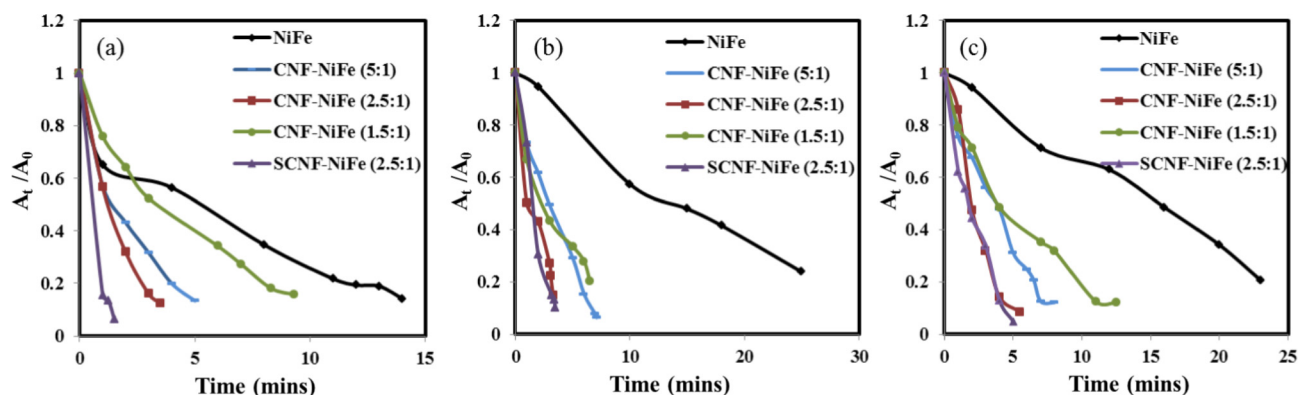


**Fig. 15**  $A_0/A_t$  vs. time graphs for the reduction of (a) 2-NP, (b) 3-NP and (c) 4-NP in the presence of NiFe and the synthesized nanocomposites as catalysts.

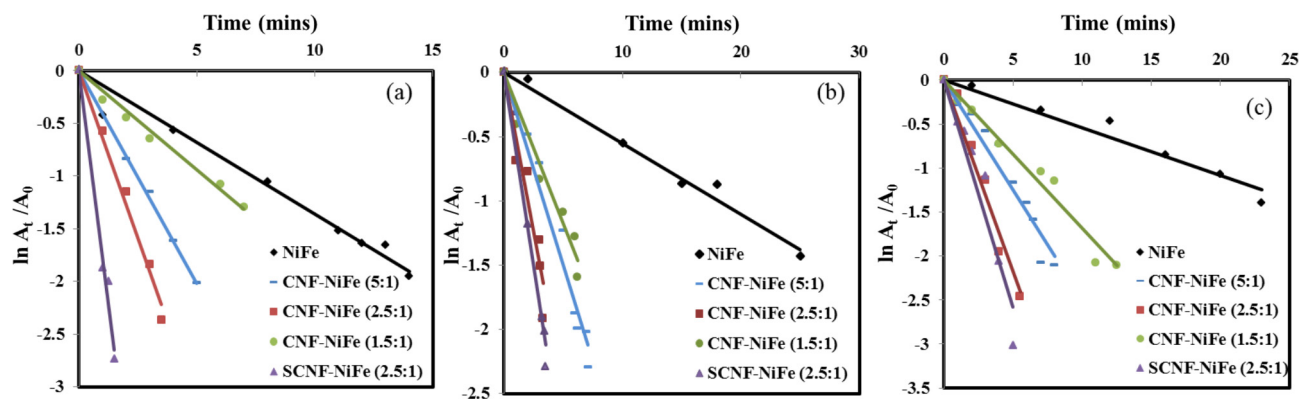


**Fig. 16**  $\ln A_0/A_t$  vs. time graphs for the reduction of (a) 2-NP, (b) 3-NP and (c) 4-NP in the presence of NiFe and the synthesized nanocomposites as catalysts.

0.055  $\text{min}^{-1}$  for 3-NP and 0.054  $\text{min}^{-1}$  for 4-NP while the rate constant values for SCNF-NiFe (2.5:1) were 1.1767  $\text{min}^{-1}$  for 2-NP, 0.606  $\text{min}^{-1}$  for 3-NP and 0.517  $\text{min}^{-1}$  for 4-NP. It can be inferred from the figure that the synthesized nanocomposites are more proficient in the reduction reaction as compared to pristine NiFe for all three nitrophenols. Again the catalytic efficiency of the synthesized nanocomposites follows the same order as in the photo Fenton degradation of dye: SCNF-NiFe

(2.5:1) > CNF-NiFe (2.5:1) > CNF-NiFe (5:1) > CNF-NiFe (1.5:1) > NiFe.

### 3.7. Mechanistic pathways

The mechanistic pathway for both the photocatalytic oxidation and reduction of organic pollutants is shown in Fig. 17. Firstly, here it is necessary to mention that CNF do not show

**Table 4** Rate constant values for the reduction of 2-NP, 3-NP and 4-NP using synthesized NiFe and synthesized nanocomposites as catalysts.

Sample	Rate Constant ( $k \times 10^{-1}$ ) ( $\text{min}^{-1}$ )		
	2-NP	3-NP	4-NP
NiFe	1.36	0.55	0.54
CNF-NiFe (5:1)	4.04	2.99	2.51
CNF-NiFe (2.5:1)	6.35	4.97	4.38
CNF-NiFe (1.5:1)	1.88	2.36	1.69
SCNF-NiFe (2.5:1)	17.67	6.06	5.17

catalytic activity for both oxidation and reduction reaction under the testing environment. Due to their inherent magnetic character, pristine NiFe nanoparticles agglomerate. The agglomeration of the pristine NiFe nanoparticles reduced their dispersability, stability and specific surface area, which are very crucial factors for the catalytic activity. In comparison, using CNF as a template avoided the aggregation of NiFe nanoparticles. The well dispersed NiFe nanoparticles on the surface of CNF made full contact with the reactant molecules which lead to enhanced catalytic performance (Wu et al., 2014). In the photocatalytic oxidation of dye, the main process responsible for the degradation is the photo Fenton process. When the catalyst is irradiated with visible light, there is generation of electron hole pair. This electron hole pair interacts with oxidant ( $\text{H}_2\text{O}_2$ ) and  $\text{OH}^-$  (from water) leading to generation of hydroxyl radicals which are the active species for dye degradation. However, the preliminary adsorption of dye molecules allows significant increase in the efficiency of degradation process due to proximity of hydroxyl radicals and the dye molecules (Riberio et al., 2016). In case of reduction reaction, when the nanocomposites were introduced as catalyst in the reaction mixture, the NiFe nanoparticles supported on CNF triggered the reduction reaction by the flow of electrons from  $\text{BH}_4^-$  to the nitrophenol molecules. Through the flow of

electrons, the nitro moiety gets converted to amino moiety and hence the reduction reaction occurs.

### 3.8. Recyclability and stability of catalyst

One of the best advantages of this non-toxic, green and efficient catalyst is its easy recovery. Successive experiments were performed to appraise the reusability of the synthesized catalyst. To determine the reusability of the catalyst, the catalyst was separated using an external magnet after completion of the reaction and then washed with water and ethanol and dried. The recyclability test was performed using SCNF-NiFe (2.5:1) for the oxidation of RB5 and for the reduction of 2-NP under the testing environment. The catalyst could be effectively used up to three cycles for both oxidation and reduction reactions. No significant change was observed in the catalytic activity up to three cycles. However, catalytic efficiency decreased after three cycles. The plots showing the recyclability of catalyst are shown in Fig. 18.

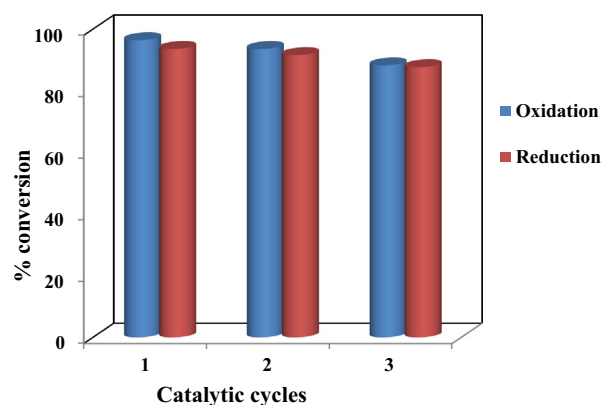


**Fig. 18** Recyclability plots for photocatalytic oxidation of RB5 and reduction of 2-NP using SCNF-NiFe (2.5:1) as a catalyst.

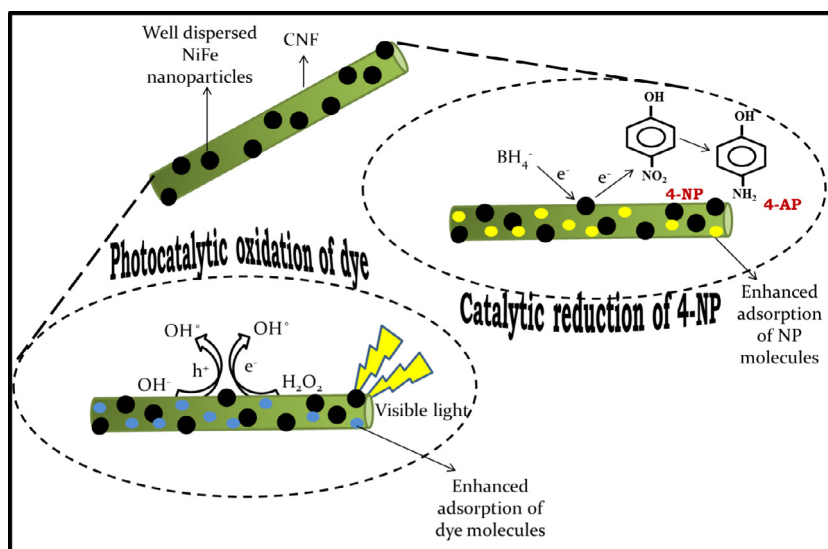


**Fig. 17** Mechanistic pathway for photocatalytic oxidation of dye and catalytic reduction of 4-NP.

#### 4. Conclusions

Cellulose based magnetically recoverable nanocomposites were successfully synthesized by a facile hydrothermal method. TEM results demonstrated that NiFe<sub>2</sub>O<sub>4</sub> nanoparticles were tightly anchored on the surface of cellulose nanofibres. The cellulose nanofibres served as an excellent template to stabilise NiFe<sub>2</sub>O<sub>4</sub> nanoparticles and prevent their aggregation. The synthesized nanocomposites proved to be excellent catalysts for both the oxidation of toxic dye and reduction of nitrophenols. Among the various nanocomposites synthesized, CNF-NiFe (2.5:1) proved to be the best one. Further silanized cellulose based nanocomposite i.e. SCNF-NiFe (2.5:1) showed enhanced catalytic activity. Facile synthesis procedure, economic source of cellulose, versatility for oxidation and reduction reaction and good reusability makes these nanocomposites economically viable and environment friendly catalyst for the mitigation of organic pollutants in aqueous medium.

#### Acknowledgements

The authors gratefully acknowledge the financial support provided by TEQIP II (Technical Education Quality Improvement Programme-II, Dr. SSB UICET, Panjab University, Chandigarh) and Council of Scientific and Industrial Research (CSIR) (Sanction No. 22(0663)/14/EMR-II). The authors are also grateful to Kunash Instruments Pvt. Ltd., Thane (W) for performing the BET analysis of the samples.

#### References

- Casbeer, E., Sharma, V.K., Li, X.Z., 2012. Synthesis and photocatalytic activity of ferrites under visible light: a review. *Sep. Purif. Technol.* 87, 1–14.
- Datta, A., Chakraborty, S., Mukherjee, S., Mukherjee, S., 2017. Synthesis of carbon nanotube (CNT)-BiFeO<sub>3</sub> and (CNT)-Bi<sub>2</sub>Fe<sub>4</sub>O<sub>9</sub> nanocomposites and its enhanced photocatalytic properties. *Int. J. Appl. Ceram. Technol.* <http://dx.doi.org/10.1111/ijac.12670>.
- Dhiman, M., Goyal, A., Kumar, V., Singhal, S., 2016. Designing different morphologies of NiFe<sub>2</sub>O<sub>4</sub> for tuning of structural, optical and magnetic properties for catalytic advancements. *New J. Chem.* 40, 10418–10431.
- Galland, S., Andersson, R.L., Salajková, M., Ström, V., Olsson, R.T., Berglund, L.A., 2013. Cellulose nanofibers decorated with magnetic nanoparticles—synthesis, structure and use in magnetized high toughness membranes for a prototype loudspeaker. *J. Mater. Chem. C* 1, 7963–7972.
- Gopiraman, M., Bang, H., Yuan, G., Yin, C., Song, K.H., Lee, J.S., Chung, I.M., Karvembu, R., Kim, I.S., 2015. Noble metal/functionalized cellulose nanofiber composites for catalytic applications. *Carbohydr. Polym.* 132, 554–564.
- Goyal, A., Kapoor, S., Samuel, P., Singhal, S., 2016. Magnetically retrievable modified nickel ferrite nanoparticles: efficient catalytic reduction of nitroarenes and photo-oxidation of hazardous dyes. *Anal. Chem. Lett.* 6, 98–123.
- Harris, V.G., Geiler, A., Chen, Y., Yoon, S.D., Wu, M., Yang, A., Chen, Z., He, P., Parimi, P.V., Zuo, X., Patton, C.E., 2009. Recent advances in processing and applications of microwave ferrites. *J. Magn. Mater.* 321, 2035–2047.
- Hossain, A.A., Rahman, M.L., 2011. Enhancement of microstructure and initial permeability due to Cu substitution in Ni<sub>0.50–x</sub> Cu<sub>x</sub> Zn<sub>0.50</sub> Fe<sub>2</sub>O<sub>4</sub> ferrites. *J. Magn. Mater.* 323, 1954–1962.
- Kaur, J., Gupta, K., Kumar, V., Bansal, S., Singhal, S., 2016. Synergic effect of Ag decoration onto ZnO nanoparticles for the remediation of synthetic dye wastewater. *Ceram. Int.* 42, 2378–2385.
- Kaushik, A., Singh, M., 2011. Isolation and characterization of cellulose nanofibrils from wheat straw using steam explosion coupled with high shear homogenization. *Carbohydr. Res.* 346, 76–85.
- Kuo, C.H., Lee, C.K., 2009. Enhancement of enzymatic saccharification of cellulose by cellulose dissolution pretreatments. *Carbohydr. Polym.* 77, 41–46.
- Liu, S., Yan, W., Cao, X., Zhou, Z., Yang, R., 2016. Bacterial-cellulose-derived carbon nanofiber-supported CoFe<sub>2</sub>O<sub>4</sub> as efficient electrocatalyst for oxygen reduction and evolution reactions. *Int. J. Hydrogen Energy* 41, 5351–5360.
- Marková, Z., Šišková, K., Filip, J., Šafařová, K., Pucek, R., Panáček, A., Kolář, M., Zbořil, R., 2012. Chitosan-based synthesis of magnetically-driven nanocomposites with biogenic magnetite core, controlled silver size, and high antimicrobial activity. *Green Chem.* 14, 2550–2558.
- Meng, Y., Chen, D., Sun, Y., Jiao, D., Zeng, D., Liu, Z., 2015. Adsorption of Cu<sup>2+</sup> ions using chitosan-modified magnetic Mn ferrite nanoparticles synthesized by microwave-assisted hydrothermal method. *Appl. Surf. Sci.* 324, 745–750.
- Nelson, M.L., O'Connor, R.T., 1964. Relation of certain infrared bands to cellulose crystallinity and crystal lattice type. Part II. A new infrared ratio for estimation of crystallinity in celluloses I and II. *J. Appl. Polym. Sci.* 8, 1325–1341.
- Nishino, T., Matsuda, I., Hirao, K., 2004. All-cellulose composite. *Macromolecules* 37, 7683–7687.
- Pang, Q., Wang, L., Yang, H., Jia, L., Pan, X., Qiu, C., 2014. Cellulose-derived carbon bearing-Cl and-SO<sub>3</sub>H groups as a highly selective catalyst for the hydrolysis of cellulose to glucose. *RSC Adv.* 4, 41212–41218.
- Park, S., Baker, J.O., Himmel, M.E., Parilla, P.A., Johnson, D.K., 2010. Cellulose crystallinity index: measurement techniques and their impact on interpreting cellulase performance. *Biotechnol. Biofuels* 3, 10.
- Parsons, P., Duncan, K., Giri, A.K., Xiao, J.Q., Karna, S.P., 2014. Electromagnetic properties of NiZn ferrite nanoparticles and their polymer composites. *J. Appl. Phys.* 115, 173905.
- Polshettiwar, V., Luque, R., Fihri, A., Zhu, H., Bouhrara, M., Basset, J.M., 2011. Magnetically recoverable nanocatalysts. *Chem. Rev.* 111, 3036–3075.
- Priyadharsini, P., Pradeep, A., Rao, P.S., Chandrasekaran, G., 2009. Structural, spectroscopic and magnetic study of nanocrystalline Ni–Zn ferrites. *Mater. Chem. Phys.* 116, 207–213.
- Riberio, K., de Andrade, T.M., Fujiwara, S.T., 2016. Preparation and application of cellulose acetate/Fe films in the degradation of reactive black 5 dye through photo-Fenton reaction. *Environ. Technol.* 37, 1664–1675.
- Rozenberg, B.A., Tenne, R., 2008. Polymer-assisted fabrication of nanoparticles and nanocomposites. *Prog. Polym. Sci.* 33, 40–112.
- Sanchez, C., Julián, B., Belleville, P., Popall, M., 2005. Applications of hybrid organic–inorganic nanocomposites. *J. Mater. Chem.* 15, 3559–3592.
- Sharma, R., Singhal, S., 2013. Structural, magnetic and electrical properties of zinc doped nickel ferrite and their application in photo catalytic degradation of methylene blue. *Physica B: Condens. Matter.* 414, 83–90.
- Sharma, R., Singhal, S., 2015. Photodegradation of textile dye using magnetically recyclable heterogeneous spinel ferrites. *J. Chem. Technol. Biot.* 90, 955–962.
- Siró, I., Plackett, D., 2010. Microfibrillated cellulose and new nanocomposite materials: a review. *Cellulose* 17, 459–494.
- Srivastava, M., Chaubey, S., Ojha, A.K., 2009. Investigation on size dependent structural and magnetic behavior of nickel ferrite nanoparticles prepared by sol–gel and hydrothermal methods. *Mater. Chem. Phys.* 118, 174–180.

- Sun, X., Yang, L., Li, Q., Zhao, J., Li, X., Wang, X., Liu, H., 2014. Amino-functionalized magnetic cellulose nanocomposite as adsorbent for removal of Cr (VI): synthesis and adsorption studies. *Chem. Eng. J.* 241, 175–183.
- Taha, A.A., Wu, Y.N., Wang, H., Li, F., 2012. Preparation and application of functionalized cellulose acetate/silica composite nanofibrous membrane via electrospinning for Cr (VI) ion removal from aqueous solution. *J. Environ. Manage.* 112, 10–16.
- Takagi, H., Asano, A., 2007. Characterization of “green” composites reinforced by cellulose nanofibers. *Key. Eng. Mater.* 334, 389–392.
- Velinov, N., Petrova, T., Tsoncheva, T., Genova, I., Koleva, K., Kovacheva, D., Mitov, I., 2016. Auto-combustion synthesis, Mössbauer study and catalytic properties of copper-manganese ferrites. *Hyperfine Interact.* 237, 1–11.
- Virkutyte, J., Varma, R.S., 2011. Green synthesis of metal nanoparticles: biodegradable polymers and enzymes in stabilization and surface functionalization. *Chem. Sci.* 2, 837–846.
- Wang, X., Xu, S., Tan, Y., Du, J., Wang, J., 2016. Synthesis and characterization of a porous and hydrophobic cellulose-based composite for efficient and fast oil–water separation. *Carbohydr. Polym.* 140, 188–194.
- Wu, X., Lu, C., Zhou, Z., Yuan, G., Xiong, R., Zhang, X., 2014. Green synthesis and formation mechanism of cellulose nanocrystal-supported gold nanoparticles with enhanced catalytic performance. *Environ. Sci. Nano.* 1, 71–79.
- Xiao, S., Gao, R., Lu, Y., Li, J., Sun, Q., 2015. Fabrication and characterization of nanofibrillated cellulose and its aerogels from natural pine needles. *Carbohydr. Polym.* 119, 202–209.
- Xiong, R., Wang, Y., Zhang, X., Lu, C., 2014. Facile synthesis of magnetic nanocomposites of cellulose@ ultrasmall iron oxide nanoparticles for water treatment. *RSC Adv.* 4, 22632–22641.
- Xu, H.L., Bi, H., Yang, R.B., 2012. Enhanced microwave absorption property of bowl-like Fe<sub>3</sub>O<sub>4</sub> hollow spheres/reduced graphene oxide composites. *J. Appl. Phys.* 111, 07A522.
- Yamaguchi, M., Kim, K.H., Ikeda, S., 2006. Soft magnetic materials application in the RF range. *J. Magn. Magn. Mater.* 304, 208–213.
- Yu, X., Kang, D., Hu, Y., Tong, S., Ge, M., Cao, C., Song, W., 2014. One-pot synthesis of porous magnetic cellulose beads for the removal of metal ions. *RSC Adv.* 4, 31362–31369.
- Zhang, N., Zang, G.L., Sh, i.C., Yu., H.Q., Sheng, G.P., 2016. A novel adsorbent TEMPO-mediated oxidized cellulose nanofibrils modified with PEI: Preparation, characterization, and application for Cu (II) removal. *J. Hazard. Mater.* 316, 11–18.
- Zhu, Y., Stubbs, L.P., Ho, F., Liu, R., Ship, C.P., Maguire, J.A., Hosmane, N.S., 2010. Magnetic nanocomposites: a new perspective in catalysis. *Chem. Cat. Chem.* 2, 365–374.